

Beam steering via resonance detuning in coherently coupled vertical cavity laser arrays

Matthew T. Johnson,^{a)} Dominic F. Siriani,^{b)} Meng Peun Tan,^{c)} and Kent D. Choquette
 Department of Electrical and Computer Engineering University of Illinois, Urbana, Illinois 61820, USA

(Received 10 September 2013; accepted 17 October 2013; published online 14 November 2013)

Coherently coupled vertical-cavity surface-emitting laser arrays offer unique advantages for nonmechanical beam steering applications. We have applied dynamic coupled mode theory to show that the observed temporal phase shift between vertical-cavity surface-emitting array elements is caused by the detuning of their resonant wavelengths. Hence, a complete theoretical connection between the differential current injection into array elements and the beam steering direction has been established. It is found to be a fundamentally unique beam-steering mechanism with distinct advantages in efficiency, compactness, speed, and phase-sensitivity to current. © 2013 AIP Publishing LLC. [<http://dx.doi.org/10.1063/1.4830432>]

Coupling between one or more oscillators occurs in numerous phenomena in photonics. One area of coupling that has been pursued for nearly three decades is that between semiconductor lasers, such as vertical cavity surface-emitting lasers (VCSELs),¹ as reviewed in Ref. 2. Coherently coupled VCSEL arrays have many features that make them viable candidates for high-radiance and optical beam steering applications.

Traditional non-mechanical beam steering methods rely on optical phase shifting of incident radiation. This is typically achieved by altering the refractive index difference between array elements, which alters the optical path length of the incident radiation traveling through the elements.³ This is illustrated in Figure 1(a) as a plane wave traveling through a graded index region. Beam steering with VCSEL arrays offers a fundamentally different approach, however, because the array acts as both the source and phase shifting mechanism, allowing maximum compactness and electro-optical efficiency. This fundamental difference has, however, limited our understanding of the physical beam steering mechanism within the arrays. Previously, the phase shift between VCSEL array elements has been shown to rely on a refractive index variation between them,⁴ which is achieved by differential current injection. Here we report the beam steering mechanism which, in contrast to all other methods, is based on a temporal phase shift between array elements at the quantum well active region. This fundamental difference is illustrated in Figure 1(b), where the phase on the right side of the source temporally lags that of the left. A similar temporal phase shift is shown to be introduced in coherently coupled VCSEL arrays by a resonance detuning between the array elements. These arrays are thus shown to harness a fundamentally unique phase-shifting mechanism, which allows record-high beam steering speeds and phase sensitivity to current injection.⁴ The beam steering can also be naturally extended into two dimensions.⁵ These advantages are

particularly applicable to miniature LADAR systems or high-speed, low-power-consumption optical communications. For example, typical modulation schemes require a differential voltage between 0.5 and 2 V, while the array shown herein can sweep its entire steering range with a differential voltage of only 100 mV. Similar arrays could thus be configured to steer on and off a receiver to achieve high-speed modulation with a low differential voltage.

The VCSEL wafer used for the arrays consists of a top p-type distributed Bragg reflector (DBR) mirror and an n-type bottom DBR on an n-type GaAs substrate. The active region located between the mirrors consists of quantum-wells emitting nominally at 980 nm. The fabrication process consists of standard photolithographic procedures. The photonic crystal hole pattern is designed to optically confine the mode within the cavities of the two array elements. The photonic crystal pattern and the mesa are formed by Freon reactive ion etching of a sacrificial SiO₂ layer, and a subsequent inductively coupled plasma reactive-ion etch. Next, a high-energy (340 keV) proton implantation with a 5×10^{14} ions/cm² dosage is conducted with an 8 μm-thick photoresist blocking layer to provide current confinement within the array elements. Subsequently, bottom n-type contacts (AuGe-Ni-Au) and top p-type contacts (Ti-Au) are deposited using conventional electron-beam evaporation and a photoresist liftoff process. The etched region outside of the mesa is then planarized with a negative tone polyimide and cured at 365 °C. This polyimide

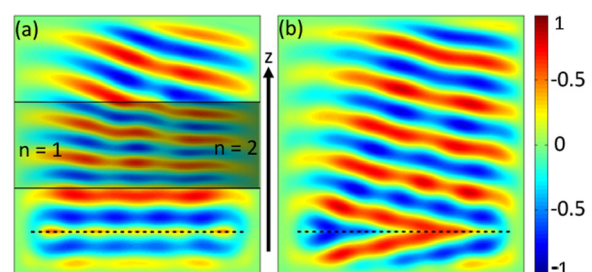


FIG. 1. Finite-difference time-domain simulation of beam steering, shown by tilted electric field profiles, with (a) spatial and (b) temporal phase shifting. The refractive index is set to one except for the region defined in (a). Dashed lines represent the source.

^{a)}matthew.johnson.9@us.af.mil. Tel.: (541)375-0906

^{b)}Present address: MIT Lincoln Laboratory, Lexington, Massachusetts 02420, USA.

^{c)}Present address: Intel Corp., Hillsboro, Oregon 97124, USA.

layer allows electrical isolation of the large fan metal contacts (Ti-Au), which are deposited next by a photoresist liftoff process. Finally, a focused ion beam is used to etch a thin line down the array center to inhibit current flow between the elements in the highly conductive top layer, improving the current confinement between elements. A sketch and scanning electron microscope (SEM) image of the 2×1 VCSEL array are shown in Figures 2(a) and 2(b), respectively.

Dynamic coupled mode theory has previously been employed to explain dynamic instability in coupled edge-emitting laser arrays and phase tuning with injection-locked vertical-cavity laser arrays.^{6,7} Here it is examined to elucidate the phase shifting mechanism observed for a 2×1 VCSEL array operating in a coherently coupled state. The electric field of element m is defined as $E_m = A_m e^{-i\Phi_m(t)}$, where A_m is the field amplitude and Φ_m is the phase. The time change of the electric field under the influence of the field from neighboring elements, E_{m-1} and E_{m+1} , can be found as^{6,8,9}

$$\frac{dE_m}{dt} = \frac{1}{2} [g(N_m - N_{th})] (1 - i\alpha) E_m + i\kappa (E_{m+1} + E_{m-1}) e^{-i\psi} + i(\omega_{coupled} - \omega_m) E_m, \quad (1)$$

where g is the differential gain, N is the carrier density, N_{th} is the threshold carrier density, α is the linewidth enhancement factor, κ is the coupling strength between elements, Ψ is the coupling phase (π for an out-of-phase array), $\omega_{coupled}$ is the coupling frequency, and ω_m is the native resonant frequency of element m . This can then be transformed into the dimensionless equations⁸

$$\frac{dX_m}{dt} = \frac{Z_m X_m}{\tau_p} - \kappa (X_{m+1} \sin(\Phi_m - \Phi_{m+1} - \psi) + X_{m-1} \sin(\Phi_m - \Phi_{m-1} - \psi)) \quad (2)$$

and

$$\frac{d\Phi_m}{dt} = \frac{\alpha Z_m}{\tau_p} - \kappa \left[\frac{X_{m+1}}{X_m} \cos(\Phi_m - \Phi_{m+1} - \psi) + \frac{X_{m-1}}{X_m} \cos(\Phi_m - \Phi_{m-1} - \psi) \right] + (\omega_{coupled} - \omega_m), \quad (3)$$

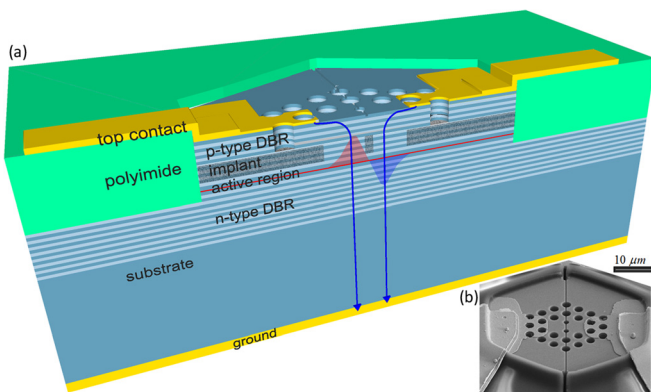


FIG. 2. (a) Sketch and (b) SEM image of 2×1 VCSEL array. Sketch shows preferred current path from the contacts and the resulting out-of-phase modal profile.

where τ_p is the photon lifetime, and X_m , Φ_m , and Z_m are the normalized magnitude, phase, and excess carrier density of element m . The following variables are used in the transformation:⁸

$$X_m = \left(\frac{1}{2} g \tau_s \right)^{\frac{1}{2}} |E_m| \quad \text{and} \quad (4)$$

$$Z_m = \frac{1}{2} g N_{th} \tau_p \left(\frac{N_m}{N_{th}} - 1 \right),$$

where τ_s is the carrier lifetime. For a two-element array ($m = 1, 2$) in steady state, Eq. (3) can be reduced to

$$\alpha(Z_2 - Z_1) = \kappa \tau_p (X_1/X_2 - X_2/X_1) \cos(\Phi_1 - \Phi_2 - \Psi) + (\omega_2 - \omega_1) \tau_p. \quad (5)$$

Z_1 and Z_2 can then be obtained from Eq. (2) and substituted into Eq. (5) to yield

$$\omega_2 - \omega_1 = -\kappa \left[\alpha \left(\frac{X_1}{X_2} + \frac{X_2}{X_1} \right) \sin(\Phi_1 - \Phi_2 - \Psi) + \left(\frac{X_1}{X_2} - \frac{X_2}{X_1} \right) \cos(\Phi_1 - \Phi_2 - \Psi) \right]. \quad (6)$$

The native resonant frequency difference between elements, found on the left side of Eq. (6), thus governs the phase shift between elements found on the right side of the equation, along with some additional correlations to other parameters. Equations (2) and (3) can also be manipulated to yield the native resonant frequencies of the individual elements as

$$\omega_1 = \omega_{coupled} - \kappa \frac{X_2}{X_1} [\cos(\Phi_1 - \Phi_2 - \psi) - \alpha \sin(\Phi_1 - \Phi_2 - \Psi)] \quad \text{and} \quad (7)$$

$$\omega_2 = \omega_{coupled} - \kappa \frac{X_1}{X_2} [\cos(\Phi_1 - \Phi_2 - \psi) + \alpha \sin(\Phi_1 - \Phi_2 - \Psi)].$$

Equations (6) and (7) are compared against measured values below.

Near- and far-field measurements are taken over the locking range of a 2×1 VCSEL array for a fixed current injection of 3.6 mA into the left element (element 1), and varying current injection into the right element (element 2). Current injection into the array elements is achieved with high-precision current sources attached to the sample via micro-positioned probes. The near-field intensity images are taken with a CMOS camera, $50\times$ zoom near-IR lens, and 30 dB optical filter, as in Figure 3(a). The far-field profiles are obtained from an LD8900 goniometric radiometer as shown in Figure 3(b). This particular array is found to exhibit out-of-phase coupling, as portrayed by the sketch of the electric field profile in Figure 2(a). In this state we observe two near-field lobes separated by a null in between them, as in Figure 4(a). In the far-field, where the distance from the

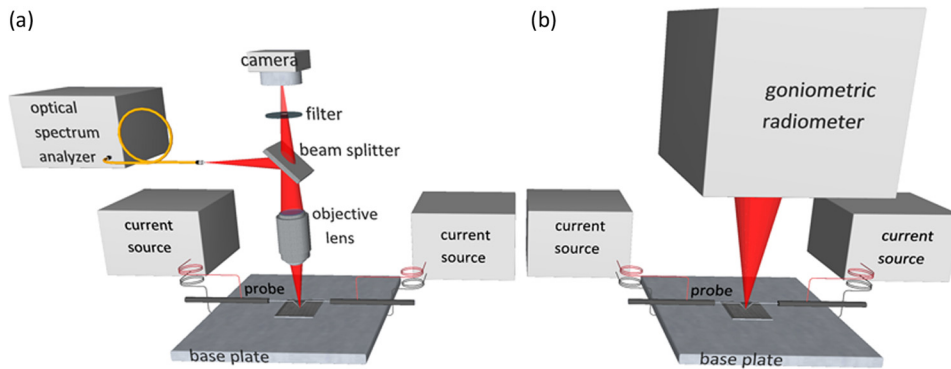


FIG. 3. Experimental setups used to obtain (a) near-field, spectral and (b) far-field data.

source is several orders of magnitude larger than the element size, we similarly observe two lobes with an on-axis null in between them, as in Figure 4(c).

The near-field amplitude profiles were obtained as the square root of the measured intensity profiles after subtracting out the background noise. The near field was then separated into two apertures, as delineated by the red line in Figure 4(a). The near-field apertures are then propagated to the far field based on the Fraunhofer approximation. As discussed in Ref. 10, the relative phase of element 2, Φ_2 , is retrieved in an iterative process that continues until the relative amplitudes of the far-field lobes match those obtained experimentally. The coherence was similarly obtained by an iterative process matching the relative amplitude of the far-field minima. The propagated-fit and experimental far-field profiles are taken along the slices shown in Figures 4(b) and 4(c), respectively, and compared in Figure 4(d). High coherence between the array elements is evident by the far-field peaks and nulls that exist within the locking range of differential current injection. It can also be seen that as the current to element 2 is increased, the far field is pulled to the right, which is caused by an increasing relative phase lag in element 2.

The spatially resolved spectra of elements 1 and 2 are also obtained over the same current range. These measurements are obtained through a $62\ \mu\text{m}$ fiber placed at the image plane of the VCSEL array. The separation between elements in the image plane of $\sim 300\ \mu\text{m}$ is sufficient to acquire spatially isolated data from each element. The objective lens,

beam splitter, and fiber are moved in unison to collect the spectrum from each element. The spectral data from the left element, as shown in Figure 4(e), is offset by 0.05 nm to account for a slight change in the input power (IV characteristics) between measurements. It is seen from Figure 4(e) that only a single spectral peak is evident within the locking range. As the current to element 2 is increased further, the spectral line splits as the emission wavelength of element 2 increases to a greater extent than that of element 1. Further beyond the locking range, the elements are shown to lase almost completely independently at their respective resonant wavelengths.

Equation (6) provides the connection between the observed phase shifting and spectral splitting. The normalized fields X_1 and X_2 are determined as the total integrated amplitude measured in each near-field element. As can be seen from the near-field amplitude image in Figure 4(a), $X_1 > X_2$ at the given current difference. These amplitude values were obtained from each of the near field images corresponding to the varying current-injection values. The coupling strength is approximated from Eq. (6) as $\kappa = -\Delta\omega_{\text{max}}/2\alpha$, where $\Delta\omega_{\text{max}}$ is the maximum resonant frequency detuning within the locking range, outside of which spectral splitting is observed. The parameter α is obtained from Ref. 11, and $\Delta\lambda_{\text{max}}$ is obtained as illustrated in Figure 5(a). These values lead to the κ value given in Table I.

Within the locking range, λ_{coupled} is observed, while λ_1 and λ_2 cannot be, by definition. In order to extract the phase based on Eq. (6), we have to first estimate how λ_1 and λ_2

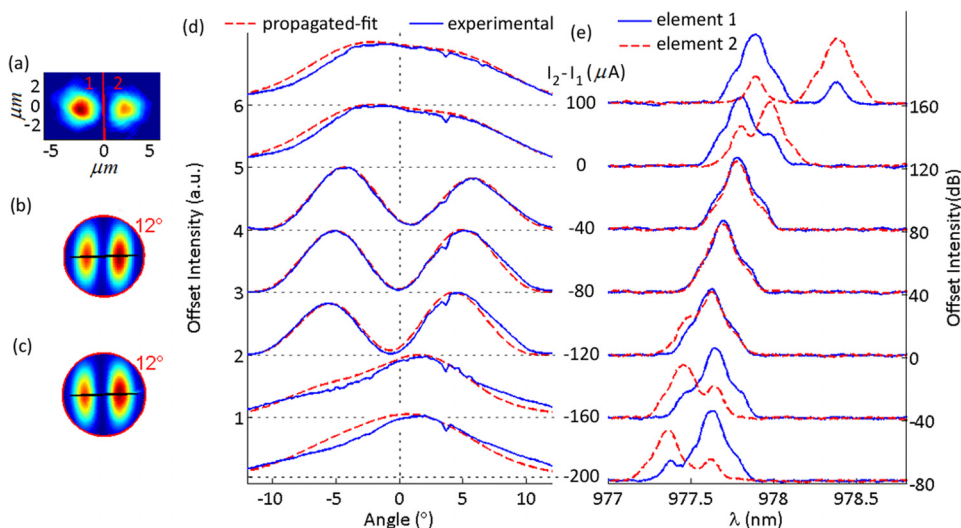


FIG. 4. (a) Near field amplitude, (b) propagated-fit, and (c) experimentally determined far-field intensity images for $I_1 = 3.6\ \text{mA}$. (d) Far field profiles are taken across the lines shown in (b) and (c) and are compared under varying differential current injection. (e) Corresponding spectra captured from elements 1 and 2, as delineated in (a).

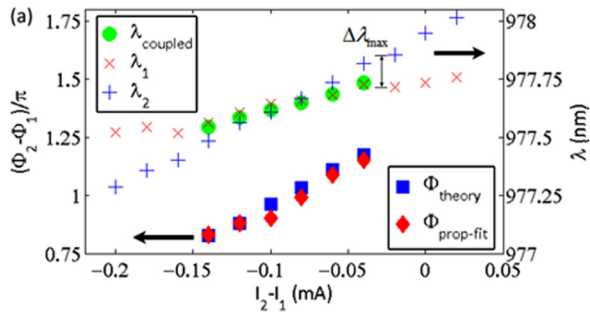


FIG. 5. Measured peak wavelength values and native resonances retrieved within the locking range. Propagated-fit phase measurements are also compared to that calculated from Eq. (6).

TABLE I. Parameters.

Ψ	α	$\Delta\lambda_{\max}$ (nm)	$\Delta\omega_{\max}$ (GHz)	κ (GHz)
Π	-5	0.136	269	26.9

vary within the locking range. Since we have these values on both sides of the locking range, we can assume the native resonances vary linearly with current within the locking range. Given this assumption, the phase values retrieved from the propagated-fit method and from Eq. (6) are compared in Figure 5. The phase values are found to match well in this array and in arrays from an alternate sample operating at 850 nm, which serves to verify the correlation of Eq. (6). While the phase variation range in this array is limited to $\sim\pi/2$, results from the 850 nm arrays show coupling phases of 0 and π with phase variation ranges approaching π .¹⁰

The native resonant wavelengths can also be retrieved with Eq. (7) using the phase extracted from the propagated-fit method. Relatively linear progressions of the native resonance wavelengths across the locking range are thus shown in Figure 5. It is also noteworthy that λ_{coupled} is found to reside closer to λ_1 because $X_1 > X_2$ across the locking range.

Previous work has shown how current injection alters the carrier and temperature distributions within the array elements, which in turn alters the refractive index profile.^{12,13} Dynamic testing has also shown that the relative phase shifting depends on this adjustment of the refractive index,⁴ although the correlation was yet unclear. Here we have employed dynamic coupled mode theory to complete the theoretical connection, as outlined in Figure 6. The index

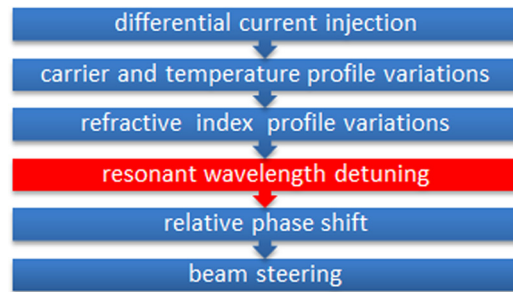


FIG. 6. Outline of progression from differential current injection to observed beam steering.

variation between elements adjusts their resonant wavelengths via $\Delta\lambda/\lambda \approx \Delta n_{\text{eff}}/n_{\text{eff}}$,¹⁴ and the resultant resonance detuning between elements causes the phase shift, per Eq. (6). The application of dynamic coupled mode theory thus elucidates the beam steering mechanism of coherently coupled VCSEL arrays. It is found to be a fundamentally unique beam-steering mechanism among those harnessed in alternate methods, and thus maintains unique advantages in efficiency, compactness, speed, and phase-sensitivity to current.

- ¹H.-J. Yoo, A. Scherer, J. P. Harbison, L. T. Florez, E. G. Paek, B. P. Van der Gaag, J. R. Hayes, A. Von Lehmen, E. Kapon, and Y.-S. Kwon, *Appl. Phys. Lett.* **56**, 1198 (1990).
- ²D. F. Siriani and K. D. Choquette, *Semiconductors and Semimetals* (Elsevier, San Diego, California, 2012), pp. 227–267.
- ³P. F. McManamon, T. A. Dorschner, D. L. Corkum, L. J. Friedman, D. S. Hobbs, M. Holz, S. Liberman, H. Q. Nguyen, D. P. Resler, and R. C. Sharp, *Proc IEEE* **84**, 268 (1996).
- ⁴M. T. Johnson, D. F. Siriani, M. P. Tan, and K. D. Choquette, *IEEE J. Sel. Top. Quantum Electron.* **19**, 1701006 (2013).
- ⁵D. F. Siriani and K. D. Choquette, *IEEE Photon. Technol. Lett.* **23**, 167 (2011).
- ⁶H. G. Winful and S. S. Wang, *Appl. Phys. Lett.* **53**, 1894 (1988).
- ⁷B. Lucke, G. Hergenhan, U. Branch, and A. Giesen, *IEEE Photon. Technol. Lett.* **13**, 100 (2001).
- ⁸H. G. Winful, *Phys. Rev. A* **46**, 6093 (1992).
- ⁹R. Lang, *IEEE J. Quantum Electron.* **18**, 976 (1982).
- ¹⁰M. T. Johnson, D. F. Siriani, J. D. Sulkin, and K. D. Choquette, *Appl. Phys. Lett.* **101**, 031116 (2012).
- ¹¹W. Schmid, C. Jung, B. Weigi, G. Reiner, R. Michalzik, and K. J. Ebeling, *IEEE Photon. Technol. Lett.* **8**, 1288 (1996).
- ¹²D. F. Siriani and K. D. Choquette, *IEEE J. Quantum Electron.* **47**, 160 (2011).
- ¹³M. T. Johnson, D. F. Siriani, P. O. Leisher, and K. D. Choquette, *Electron. Lett.* **49**, 897 (2013).
- ¹⁴G. R. Hadley, *Opt. Lett.* **20**, 1483 (1995).